

Efficient Engineering Prediction of Turbulent Wing Tip Vortex Flows

Sung-Eun Kim¹ and Shin Hyung Rhee²

Abstract: Turbulent flow past a finite wing has been computed to assess the fidelity of modern computational fluid dynamics in predicting tip vortex flows. The efficacy of a feature-adaptive local mesh refinement to resolve the steep gradients in the flow field near the tip vortex is demonstrated. The impact of turbulence modeling is evaluated using several popular eddy viscosity models and a Reynolds stress transport model. The results indicate that the combination of a computational mesh with an adequate resolution, high-order spatial discretization scheme along with the use of advanced turbulence models can predict tip vortex flows with acceptable accuracy.

Keywords: Tip Vortex, Computational Fluid Dynamics, Mesh Adaptation, Turbulence Modeling.

1 Introduction

Turbulent tip vortex flows around lifting surfaces, such as wings and propeller blades, has long been a topic of both fundamental and practical interest in the shipbuilding and aerospace industries because of its impact on various aspects of hydro- and aerodynamic performance. Despite the long history of such discussion, the task of numerically predicting tip vortex flows around lifting surfaces remains difficult.

Of the several challenges to be resolved before the subject flow can be predicted accurately, we focus on two. First, the sheer numerical difficulty of resolving the large gradients in the flow fields of the boundary layer on the lifting surfaces and the tightly braided vortices emanating from the tip needs to be overcome. One difficulty constantly encountered in real applications is the presence of many such regions that require high resolution. Moreover, when there is a need to trace tip

¹ Naval Surface Warfare Center Carderock Division, W Bethesda, MD, U.S.A.

² Corresponding author, Dept. of Naval Archi. & Ocean Eng., Research Inst. of Marine Systems Eng., Seoul National Univ., 599 Gwanang-no, Gwanak-gu, Seoul, 151-744, Korea. Email: shr@snu.ac.kr

vortices over a long distance, as may be the case when tracking the trailing vortices in an aircraft wake, the difficulty becomes more acute.

The presence of multiple features with widely varying length scales translates into a challenge in meshing. The question then becomes how to allocate computational elements in the solution domain to obtain the best possible solution accuracy, while maximizing the “return on investment” in terms of computational resource usage. Global mesh refinement, i.e., refining the mesh everywhere, is a computationally expensive proposition for three dimensional flows. Fortunately, one promising solution is offered by undertaking local mesh refinement with coarsening based on the solution itself, for example, Lucas et al. (2009). This requires, however, numerical methods capable of handling unstructured meshes.

Second, and arguably the most difficult of the challenges, is turbulence modeling. Typical lifting surface flows involve a strongly non-equilibrium boundary layer that undergoes a rapid change from the moment it impinges on the wall until it leaves the surface in the form of a free vortex sheet. Furthermore, the flow off the wall is dominated by strong rotation near the tip vortices. As is well-known, isotropic eddy viscosity-based turbulence models are less than adequate to handle this kind of flow. All of this begs the question: what level of turbulence modeling is needed for accurate prediction of lifting surface flows, or in other words, what are the impacts on accuracy of using different turbulence models. As an example, our earlier study of turbulent flow past a 6:1 spheroid at incidence revealed that a second moment closure model based on solution of the Reynolds stress transport equations resulted in a remarkably accurate prediction of this vortex dominated flow, outperforming all eddy viscosity models (Kim et al., 2003).

In the present study, we conducted a computational study on the flow around a generic finite wing configuration. The flow was studied in the wind tunnel at the NASA Ames Research Center (Chow et al., 1993; Chow et al., 1997) with a focus on the tip vortex generated around a wing placed at an angle of attack of 10° . That moderate incidence avoids massive, unsteady separation. The mean flow and turbulence measurements shed light on the formation and evolution of the tip vortex; thus providing a useful dataset for computational fluid dynamics (CFD)-based validations. There have been previous numerical studies on this same flow (Dacles-Mariani et al., 1993, 1995, 1996; Chen, 2000; Uzun et al., 2006; Churchfield and Blaisdell, 2009). In many of the earlier studies, one-equation eddy viscosity turbulence models were used in conjunction with high-order upwind finite difference schemes. Later, Dacles-Mariani et al. (1996) showed that a prediction using the modified Spalart and Allmaras’ turbulence model (Dacles-Mariani et al., 1995) on a relatively fine mesh (2.5×10^6 cells) closely matched the experimental data. However, the minimum static pressure along the tip vortex core was still apprecia-

bly under-predicted. Some latest studies show that more complicated turbulence closure on highly refined meshes is indeed helpful to achieve academically oriented high fidelity solutions (Uzun et al., 2006; Churchfield and Blaisdell, 2009), although it is doubtful how easily such practices can be applied in real-world engineering problems. There are other advanced methods and techniques reported to be superb for highly turbulent flows with strong vortices, which should be considered in the future as more powerful computational resources become available. Examples include the large eddy simulation (LES) formulation combined with immersed boundary method (da Silva et al., 2009), and the explicit algebraic Reynolds stress model (Naj ad Mompean, 2009).

This study addresses the aforementioned two challenges. First, we assess the potential of feature-adapted local mesh refinement to resolve the formation and evolution of the tip vortex. A systematic, global mesh refinement study was also conducted to provide a basis for comparisons and accuracy estimation. Second, the impact of turbulence modeling is investigated using three contemporary two-equation eddy viscosity models and a differential Reynolds stress model.

The paper is organized as follows. The description of the physical problem and its experiment is presented in section 2, followed by the numerical method, turbulence modeling, computational domain and mesh, and boundary conditions in sections 3 to 6, respectively. The computational results are presented and discussed in section 7. Finally, section 8 provides the summary and conclusions.

2 Wing model and experiment

The model in the experiment was a finite wing with a chord length (c) of 1.212 m and a span length (s) of 0.909 m. The wing is a rectangular platform mounted on the tunnel bottom at a 10° incidence to the free stream. The inflow velocity measured in the experiment was 51.51 m/sec, sufficiently low to be considered incompressible. The Reynolds number, based on c and the free stream velocity, is 4.6×10^6 . The boundary layer is tripped along the leading edge. The wind tunnel had a 1.221 m \times 0.814 m cross section, which creates a significant blockage effect.

Among the large experimental datasets, we focused the measurement area on the near-field region close to the wing tip and the wake. Mean velocity, pressure (static and total), and turbulent stresses were measured extensively on several crossflow planes. The measurements revealed an exceptionally large axial velocity reaching a maximum of nearly 1.8 times the free stream velocity, a pronounced low (negative) static pressure peak, and high levels of turbulent stresses along the vortex core. A kink in the vortex axis was observed downstream of the trailing edge, which is likely due to the merger of the primary vortex with a secondary vortex. The mea-

surements also showed that the turbulent shear stress contours had a characteristic pattern that resembles a four-leaf clover tilted by 45° from both the vertical and horizontal axes, indicating a misalignment between the turbulent stress and mean strain rates.

3 Numerical method

All of the computations presented here were carried out using the commercially available CFD simulation software, FLUENT v6.3. The flow was assumed incompressible. A cell-centered finite volume method was adopted in conjunction with a linear reconstruction scheme capable of handling both structured and unstructured meshes. Gradients of the solution variables were computed using the Green-Gauss' theorem. Diffusion terms were discretized using a second-order central differencing scheme. For convective terms, the QUICK scheme was used. The discretized equations were solved using a pointwise Gauss-Seidel iteration in conjunction with an algebraic multi-grid method to accelerate convergence of the solution. Similar methods were successfully applied to performance analysis of a tidal stream energy conversion turbine recently (Jung et al., 2009). The details of the numerical method can be found in the references (Mathur and Murthy, 1997; Kim et al., 1998).

4 Turbulence modeling

Among the more widely used eddy viscosity turbulence models, such as those in the $k-\varepsilon$ and $k-\omega$ families and the Spalart-Allmaras (SA) one-equation model (Spalart and Allmaras, 1992), we selected a few representative models to keep the scope of the study manageable. In addition, and for the reasons alluded to in section 1, we included a second moment closure model in the study. In the following, we briefly describe the turbulence models chosen for use in the present study.

4.1 Eddy viscosity models

We selected three of the more popular eddy viscosity models for this study. Based on its popularity in the ship hydrodynamics and aerodynamics communities, the SA model was chosen. We also adopted the SA modification proposed and used by Dacles-Mariani et al. (1995, 1996) which suppresses the unduly large build-up of eddy viscosity in the vortex core. That modification employs the following strain rate to compute the production term.

$$\hat{S} = \Omega + C_{prod} \min [0, S - \Omega] \quad (1)$$

where $C_{prod} = 2.0$ and S and Ω are the moduli of the strain rate and the rotation rate tensors, respectively.

Among the $k-\varepsilon$ family of turbulence models, the realizable $k-\varepsilon$ model (*RKE* hereafter) of Shih et al. (1995) was chosen based on its good reputation for non-equilibrium boundary layer flows. Here, for computations employing a fine near-wall mesh, the model, which was originally formulated as a high Reynolds number model, had to be modified to account for the near-wall effects. To that end, a zonal hybrid model was used. Lastly, the shear stress transport (SST) $k-\omega$ model, described by Menter (1994), was selected to represent the $k-\omega$ family.

4.2 Reynolds stress transport model

The Reynolds stress transport model (RSTM) used in this study largely reflects the model used by Gibson and Launder (1978). The near wall, low-Reynolds number effects were modeled using the approach of Launder and Shima (1989). The details of the model used here have been described by Kim (2001). The RSTM used has been validated for a number of complex internal and external flows (Kim, 2001; Kim and Rhee, 2002).

5 Computational domain and mesh

In view of the relatively simple geometry, hexahedral cell meshes with an O-H topology were used in this study. The solution domain and a partial view of the meshes are shown in Figure 1. The computational domain is bounded by the tunnel walls (top, bottom, and side walls), the inflow boundary located approximately $1.5c$ upstream of the leading edge, and the exit boundary at about $3.6c$ downstream from the trailing edge. Four meshes with varying resolutions were used (Table 1). The first three meshes (*Mesh I*, *Mesh II*, and *Mesh III*) were obtained by globally refining the coarsest one (*Mesh I*). The value of y^+ in the finest mesh (*Mesh III*) was approximately 1.0 for those cells adjacent to the wing surface. However, the mesh resolution near the tunnel walls was coarser, and the y^+ value at those locations was high enough to invoke the log-law as a wall boundary condition.

Table 1: Meshes used for the computations

	Number of elements	Remarks
Mesh I	385,000 cells	coarsest
Mesh II	1,040,000 cells	globally refined
Mesh III	2,300,000 cells	globally refined
Mesh IV	1,380,000 cells	locally refined

In addition, we employed a locally adapted mesh (*Mesh IV*). Our intention was to evaluate a feature-adaptive mesh refinement in which cells are refined when the

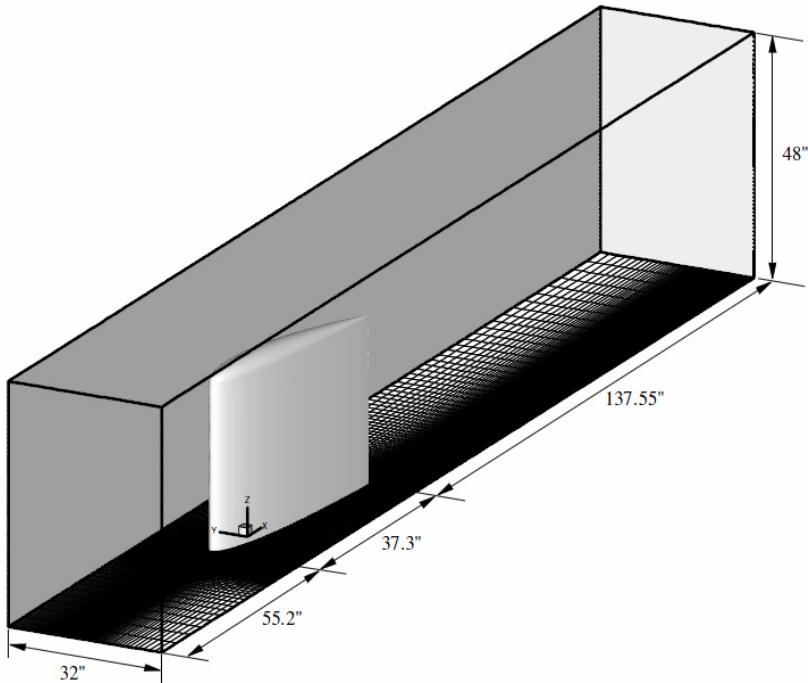


Figure 1: Solution domain and partial view of the mesh

value of a selected variable at the cells falls within a specified range. Implementation of this approach allows the choice of any quantity from among the solution variables (e.g., velocity components, pressure, k , ε , etc.) or any derived quantity based on the solutions (e.g., derivatives, curvatures, vorticity, helicity, total pressure, etc.). For the flow assessed here, any flow variable that can demarcate the tip vortex region was deemed a good candidate feature for local adaptation.

The second invariant of the deformation tensor, defined as

$$Q = \frac{1}{2} (\Omega^2 - S^2) \quad (2)$$

is a plausible choice, inasmuch as the vortex core, where rotation rate dominates over strain rate, can be identified as the region with a positive Q . The idea of local refinement based on this second invariant is illustrated in Figure 2(a), which shows the cells marked for refinement. In that example, the medium mesh (*Mesh II*), along with its solution, was used for feature adaptation, resulting in a 1.8×10^6 cell

mesh. The figure shows that the cells marked for refinement largely occupy the region around the tip vortex.

Static pressure is an equally plausible choice for an invariant, considering that a tip vortex has a very low static pressure along its core. Figure 2(b) shows the cells marked for refinement based on the static pressure coefficient (C_p), starting from *Mesh II*. It can be seen that the cells marked for refinement overlap the region near the tip vortex. That C_p feature-adapted mesh had approximately 1.4×10^6 cells, markedly lower than the cell count a global refinement would yield. In the present study, we used this mesh (*Mesh IV*).

Admittedly, the choice of the quantity used to detect the adaptive feature is arbitrary and requires a considerable knowledge of the flow on the part of the users. This usability problem becomes serious for complex industrial applications in which the predictions are most likely to be sensitive to the choice of the variable. Thus, local refinement or coarsening of meshes, using rigorously derived error indicators as adaptation criteria, may be a better alternative.

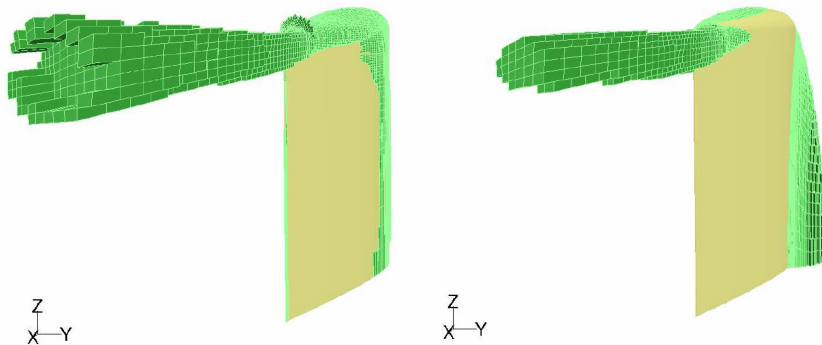


Figure 2: Cells marked for local refinement based on flow variables: (a) second-invariant (left); (b) static pressure coefficient (right)

6 Boundary conditions

Some earlier numerical studies (Dacles-Mariani et al., 1995) used experimental data to specify Dirichlet type boundary conditions not only on the inlet but also on the outlet boundary. However, using a Dirichlet type boundary condition on the outlet, which is generally not known a priori, is questionable, both mathematically and practically.

Here, for simplicity, the free stream velocity was specified at the upstream inlet boundary. That approach was deemed justifiable as our focus was on the region away from the tunnel wall. The exit boundary was modeled as a pressure outlet on which an area-averaged static pressure can be specified. The velocity on the pressure outlet was linearly extrapolated from the adjacent interior cells so that overall continuity (i.e., mass conservation) could be satisfied. Other solution variables (e.g., turbulence quantities) have been extrapolated in a similar manner.

On both the tunnel wall and the wing surface, we adopted a generalized wall function approach that invokes wall laws that depend on the y^+ value to provide the wall boundary conditions for both the momentum and turbulence equations. The appropriate laws were applied to the entire inner layer, including the viscous sub-layer, the buffer zone, and the logarithmic layer.

7 Results and discussion

Figures 3 – 6 show the negative peak C_p , the maximum axial velocity magnitude, and the y - and z -coordinates, respectively, along the vortex core as predicted by the *RSTM*. The results exhibit considerable mesh dependency. When viewing these results, however, note that the local extrema of the static pressure and the axial velocity magnitude appear more sensitive to the use of mesh resolution than the overall error norms. The figures show that the coarsest mesh, *Mesh I*, captures the major qualitative features of the flow; however, the static pressure and the maximum axial velocity, which are measures of the strength of the tip vortex, have been severely under-predicted. The results from the finer meshes show a typical mesh convergence of the solutions, although the convergence rate is rather slow. The finest mesh, *Mesh III*, provided good predictions of all aspects of the flow. Moreover, the static pressure and the velocity excess along the core of the tip vortex were accurately predicted, although the predictions gradually deviated from the wake measurements. Figures 5 and 6 show that the location of the vortex core has been captured by the predictions. Interestingly, the “kink” or sudden change in the vertical location (z -coordinate) of the vortex axis observed by Chow et al. (1993) was also seen in our predictions.

The same figures show results that were obtained with the locally adapted mesh (*Mesh IV*). Despite the lower number of cells (1.4×10^6 cells) using *Mesh IV* than when using the finest mesh (*Mesh III*; 2.3×10^6 cells), the *Mesh IV* accuracy was similar to that of *Mesh III*.

Figures 7(a) and 7(b) depict the contours of the C_p and the axial velocity magnitude at a selected number of crossflow planes as predicted by the *RSTM* with *Mesh III*. Figures 8(a) and 8(b) depict an overall impression of the corresponding static

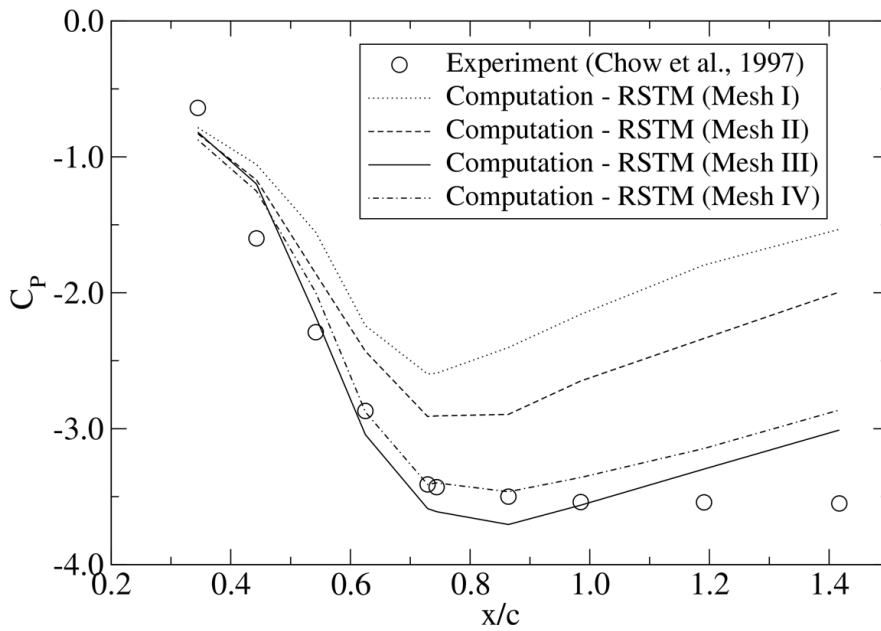


Figure 3: Mesh dependency of RSTM results for minimum static pressure along vortex core

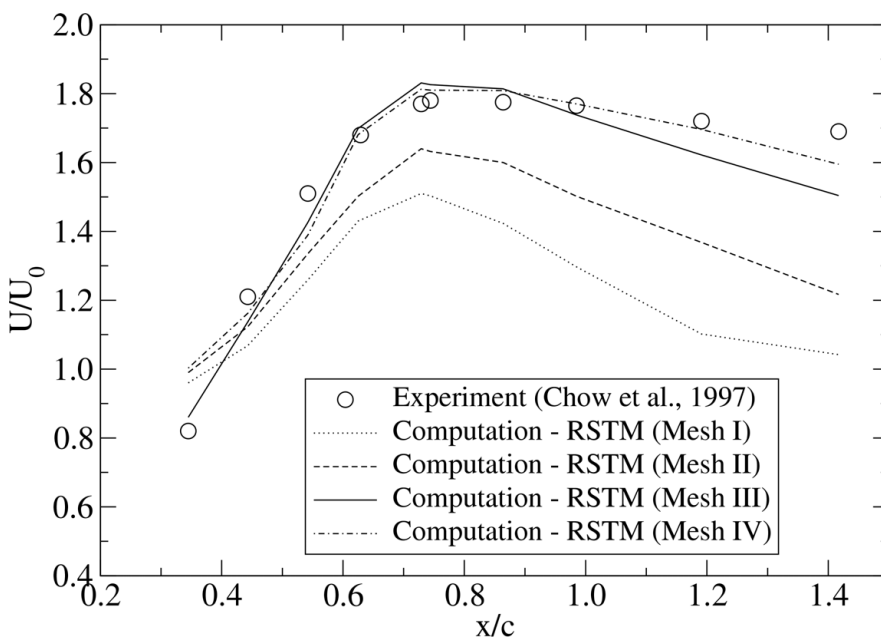


Figure 4: Mesh dependency of RSTM results for maximum axial velocity along vortex core

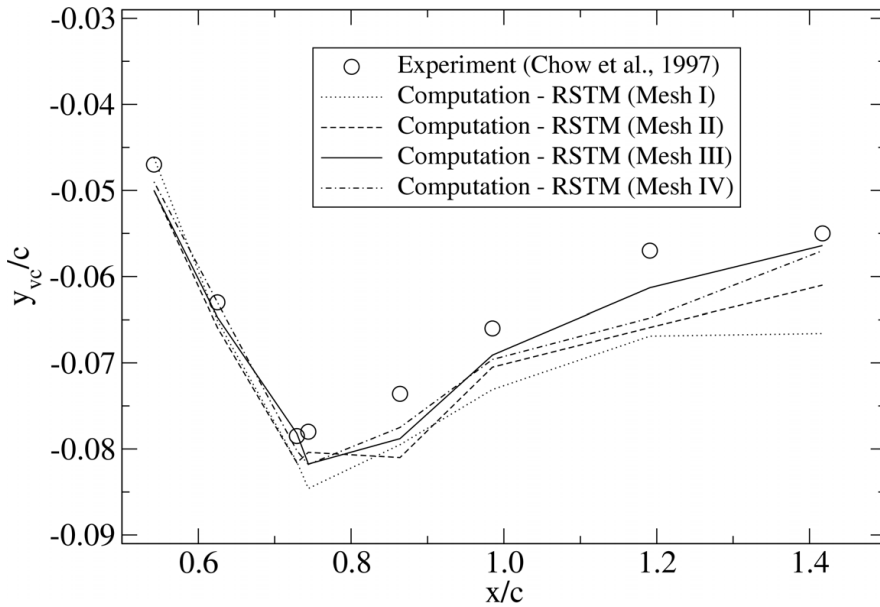


Figure 5: Mesh dependency of RSTM results for y-coordinates of vortex core

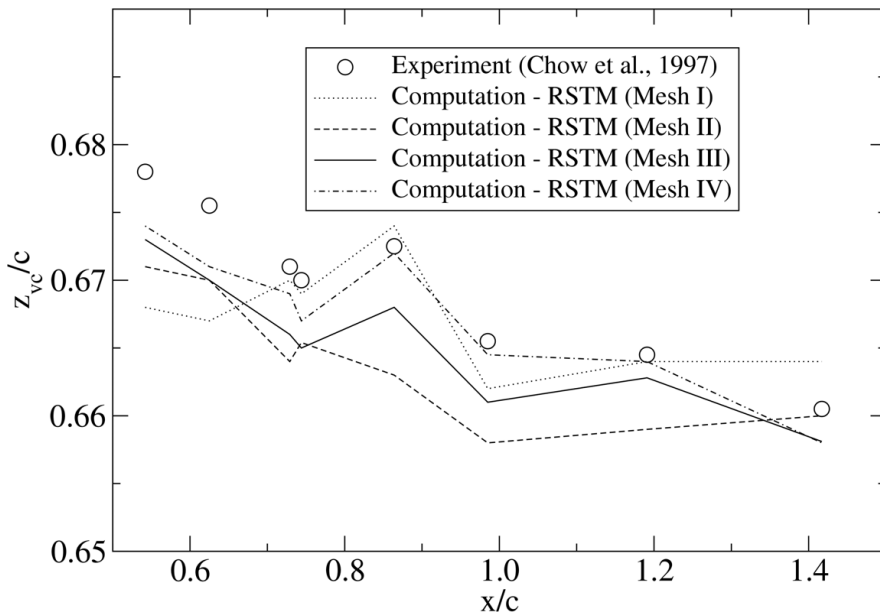


Figure 6: Mesh dependency of RSTM results for z-coordinates of vortex core

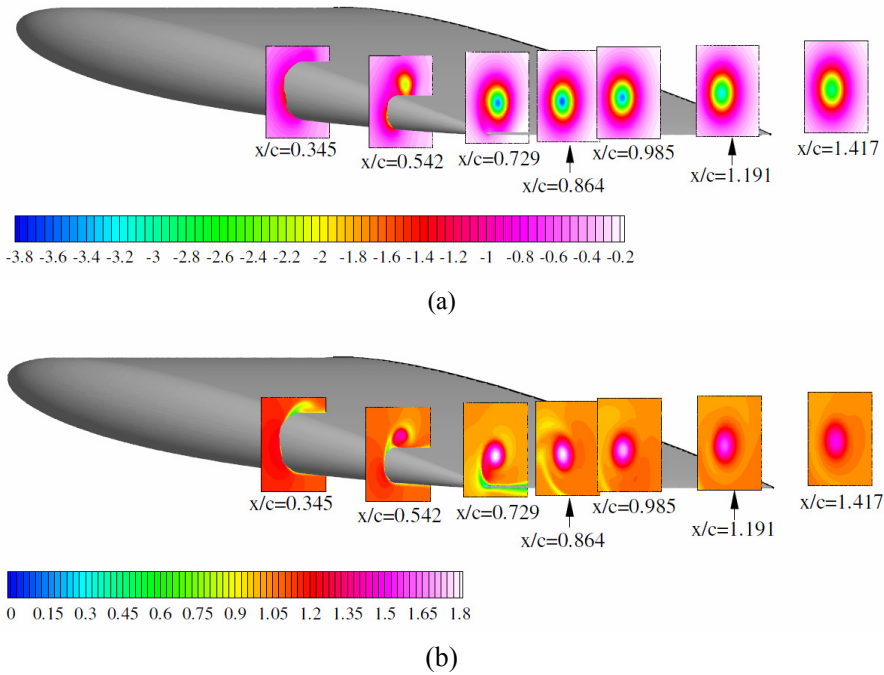


Figure 7: (a): Static pressure coefficient contours at crossflow planes predicted using RSTM; (b): Axial velocity magnitude contours at crossflow planes predicted using RSTM

pressure distribution on the wing surface. A characteristic surface pressure distribution pattern, including a region of low pressure on the suction side near the wing tip, i.e., the footprint of a tip vortex, was well captured by the *RSTM* on *Mesh III* prediction.

The aforementioned kink in the axis of the vortex core, observed slightly downstream of the trailing edge, has been attributed to the merging of primary and secondary vortices. The pathlines, traced using the *RSTM* prediction shown in Figure 9, appear to support that hypothesis. In the figure, the pathlines have been colored according to the axial component of the vorticity vector. The figure shows the presence of a secondary vortex (with a rotation opposite to that of the primary vortex; as show in red) that merges with the primary vortex slightly behind the trailing edge, i.e., where the kink may be observed.

The *RSTM* offers an opportunity to make direct comparisons of predicted and mea-

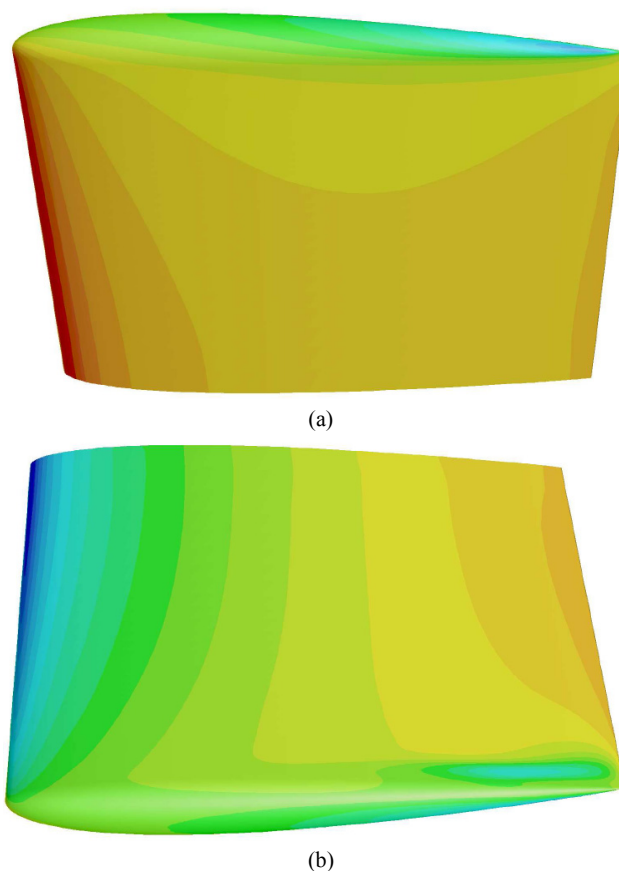


Figure 8: (a): Surface static pressure distribution on pressure side predicted by *RSTM* on Mesh III (Contour range $-1 \leq C_p \leq 1$ with interval of 0.2); (b): Surface static pressure distribution on suction side predicted by *RSTM* on Mesh III (Contour range $-1 \leq C_p \leq 1$ with interval of 0.2)

sured Reynolds stresses. Here, it was found that the *RSTM* predictions underestimate the normal and shear stresses near the vortex core at all crossflow planes where measurements were made. Nonetheless, the overall trends observed in the experiment were closely reproduced by the predictions. Figure 10 depicts the contour of one of the shear stresses predicted using the *RSTM*, and shows the characteristic pattern (resembling a four-leaf clover tilted about 45° off the vertical and horizontal axes), as was found in a previous experiment (Chow et al., 1993).

Comparisons of the results from the three eddy viscosity turbulence models (*SA*,

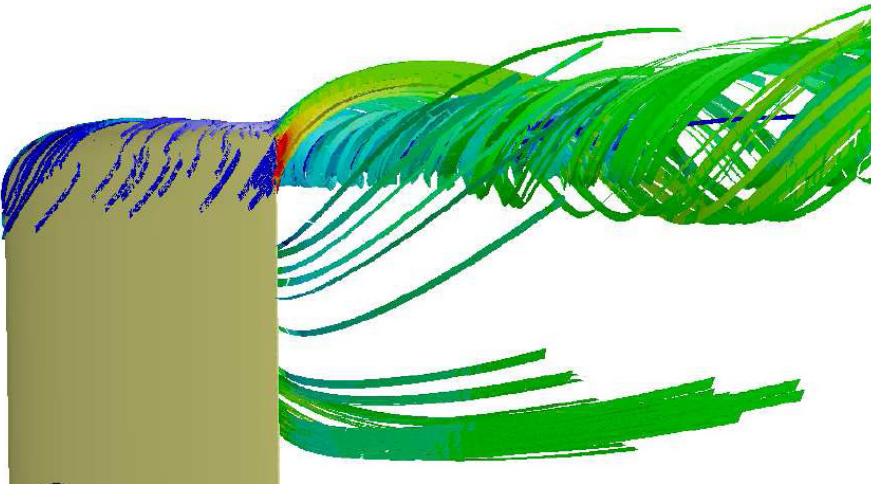


Figure 9: Pathlines in tip region colored by axial component of vorticity vector (Contour range $-300 \leq \omega \leq 300$ with interval of 30)

RKE, *SST*) and the *RSTM* are presented in Figures 11 and 12. As shown, the *RSTM* gave the best result. What is intriguing is the remarkable performance of the *SA* model, a performance level that is largely consistent with the finding reported by Dacles-Mariani et al. (1996). Compared to the *SA* result of Dacles-Mariani et al. (1996), our *SA* result for the minimum static pressure measurement along the vortex core is more accurate. Their result under-predicted the negative peak pressure along the vortex core by >11 % on average, whereas our *SA* result over-predicted the negative peak static pressure near the trailing edge by a few percent, albeit our results showed a faster recovery in the wake.

It is noteworthy that the four turbulence models predicted different peak values and rates of recovery for both the static pressure and the axial velocity in the wake. Overall, however, the *RSTM* indicated the slowest recovery rate, which agrees with the experimental data.

It comes as little surprise that the *RKE* and the *SST* model prediction accuracies were much poorer than those of the *SA* model. All indicators suggest that two-equation models, which are arguably more sophisticated and more advanced, predict a substantially weaker tip vortex, resulting in a less pronounced negative pressure peak and a smaller velocity excess than in the *SA* model.

The high predictive accuracy of the *SA* model for this flow is related to the reduced level of eddy viscosity in the vortex core, which in turn is the result of the modi-

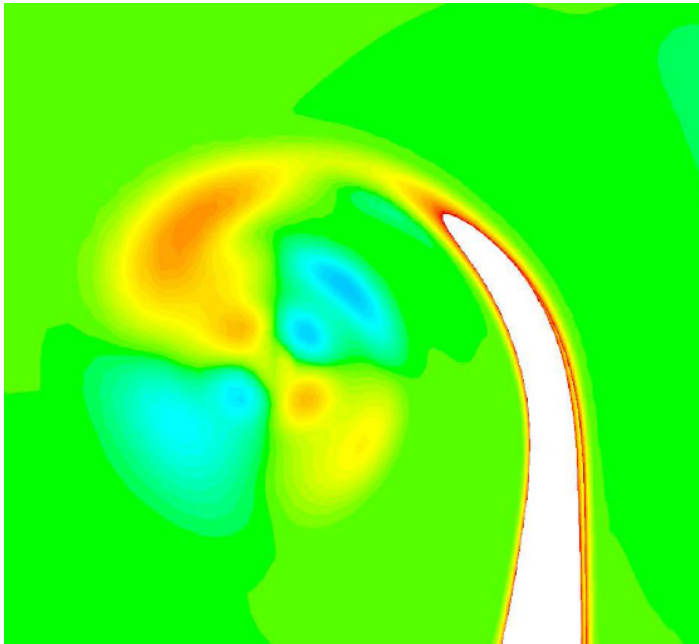


Figure 10: Contours of Reynolds shear stress component, $v'w'$, distribution at $x/c = 1.420$ (Contour range $-2000 \leq v'w' \leq 2000$ with interval of 200)

fication presented in Equation (1). It can be shown that eddy viscosity production ($P \approx v_r \hat{S}$) becomes negative when $S/\Omega < 0.5$. Because of this, turbulent viscosity is destructed along the core of the tip vortex, when the rotation rate is much larger than the strain rate, as illustrated in Figure 13. That figure depicts an iso-surface of $S/\Omega = 0.3$, colored to show the production of turbulent viscosity, and clearly indicates that the $S/\Omega < 0.5$ region coincides with the vortex core.

The *RKE* model has a similar provision that reduces the production of turbulent kinetic energy via the model's C_μ parameter, which is sensitized to rotation. That provision may be the reason why the *RKE* model outperformed the *SST* model. It should be noted, however, that all of these model modifications, which have been adopted to mimic the stabilizing effects of rotation (or curvature) in the isotropic eddy viscosity framework, are ad hoc. The real physics that are associated with rotating flows like the tip vortex in this study can only be rigorously represented by a second moment closure computation; thus, explaining the success of the *RSTM* for the present flow and, presumably, for other similar vortex dominated flows.

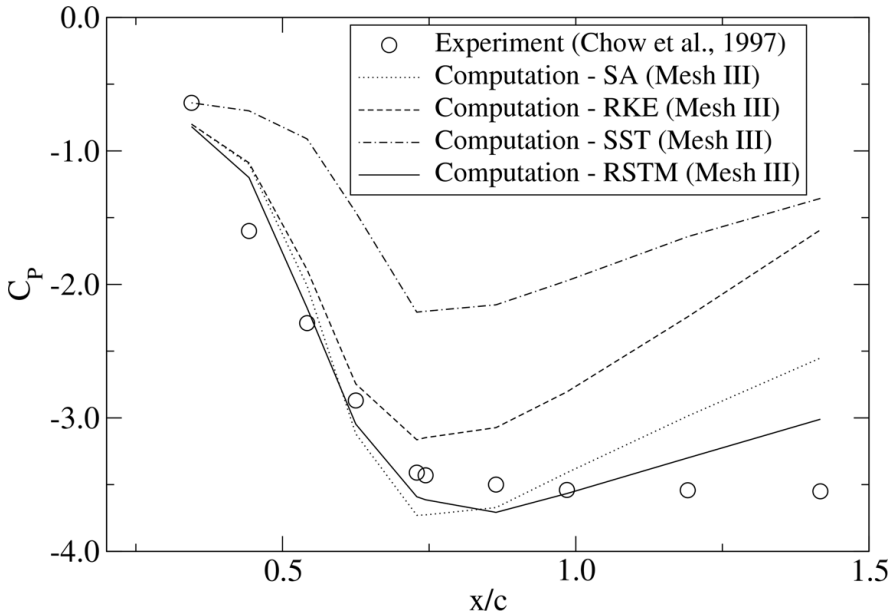


Figure 11: Minimum static pressure along tip vortex core predicted by four different turbulence models

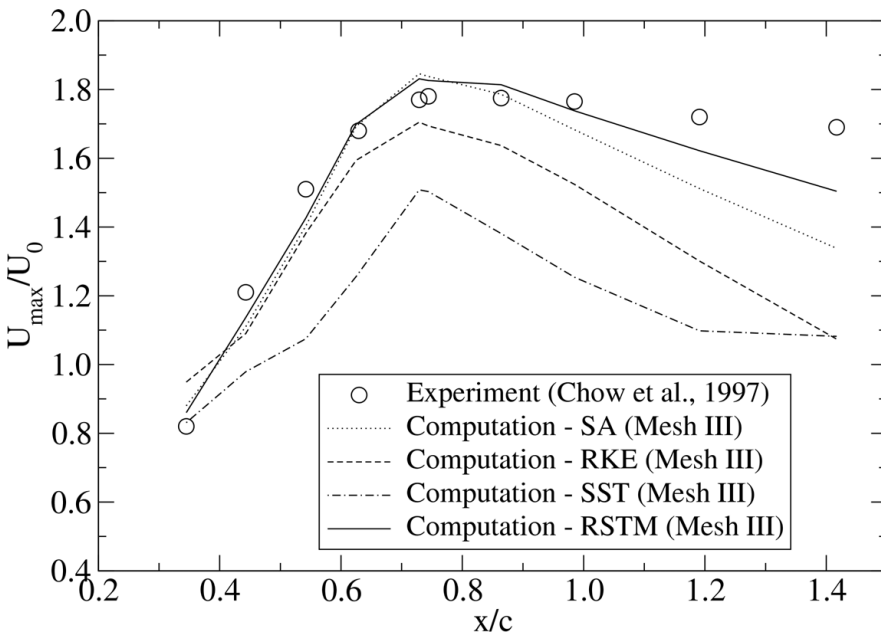


Figure 12: Maximum axial velocity along tip vortex core predicted by four different turbulence models

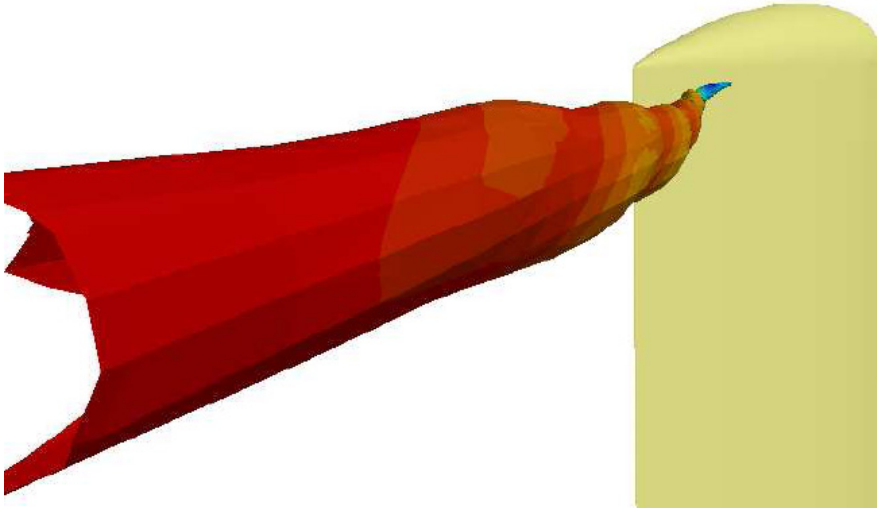


Figure 13: Iso-surface of $S/\Omega = 0.3$, colored by production of turbulent viscosity

8 Summary and conclusions

Turbulent flow past a finite-wing was studied numerically to assess the capability of modern CFD tools to capture the salient features of a lifting surface flow. Emphasis was placed on the level of accuracy with which the tip vortex can be captured. One challenge to such tools' predictive accuracy is that the flow considered here, and for lifting surface flows in general, have multiple features with widely varying length scales. This poses a computational challenge in terms of numerical resolution. To resolve the large solution gradients near a tip vortex or any other significant feature requires extremely dense clustering of the computational cells at many different parts of the solution domain. Another challenge is the complex physics involved in a vortex-dominated flow, which makes turbulence modeling difficult.

Here, we present computational results obtained using four different turbulence models: a one-equation eddy viscosity model (*SA*), two different two-equation turbulence models (*RKE*, *SST*), and a second moment closure model (*RSTM*). The computational mesh was progressively refined to establish the grid convergence of the numerical solutions, resulting in three globally refined meshes. In addition, taking advantage of the capability of CFD to handle unstructured meshes including hanging nodes, we evaluated the efficacy of a so-called feature-adaptive local mesh refinement in which the computational cells are refined when user-specified

refinement criteria are satisfied.

To summarize, the use of two different computational meshes (either the finest mesh or the locally refined mesh) and two turbulence models (*RSTM*, *SA*) predicted the salient features of the tip vortex, such as the minimum static pressure and the axial velocity excess at the vortex core, with acceptable accuracy. Particularly interesting was the finding that the computation with the locally refined mesh yielded remarkably good results, in spite of its low cell count. Furthermore the locally refined mesh results closely matched the accuracy produced using the finest globally-refined mesh. While far from being perfect, mainly due to an issue of usability in practical applications, this feature-adaptive local refinement method has sufficient merit to warrant further investigation.

With regard to turbulence modeling, the second moment closure model (*RSTM*) produced the best results; a result that was anticipated in view of the salient flow physics within the subject flow that can be rigorously modeled only by second moment closure computations. However, the modified Spalart-Allmaras model performed with relatively high accuracy, despite the ad hoc nature of the modification to mimic the stabilizing effects of rotation near the vortex core. It was observed that strong rotation near the vortex core results in locally negative turbulent viscosity production, significantly reducing turbulent diffusion and preventing the vortex from being smeared. Both Menter's $k-\omega$ model (*SST*) and the realizable $k-\epsilon$ model (*RKE*) performed poorly, substantially under-predicting the strength of the tip vortex.

Based on the present study, it is concluded that tip vortices, which are one of the most prominent aspects of lifting surface flows and have been perceived as difficult to tackle numerically, are computationally manageable using modern CFD. Furthermore, their features can be predicted with acceptable accuracy.

Acknowledgement: The second author acknowledges the support by the World Class University (R32-10161) and the National Research Foundation of Korea (NRF) grant (20090083510), funded by the Korea government.

References

- Chen, B.** (2000): RANS simulations of tip vortex flows for a finite-span hydrofoil and a marine propeller. *Ph. D. Thesis, Dep. of Mech. Eng., Univ. of Iowa.*
- Chow, J.S.; Zilliac, G.G.; Bradshaw, P.** (1993): Measurements in the near-field of a turbulent wingtip vortex. *AIAA Paper 93-0551, Proc. 31st AIAA Aerosp. Sci. Meet. and Exhib., Reno, NV.*
- Chow, J.; Zilliac, G.; Bradshaw, P.** (1997): Turbulence measurements in the near-

field of a wingtip vortex. *NASA Tech. Memo. 110418*.

da Silva, A.R.; Silveira-Neto, A.; Rade, D.A.; Francis, R.; Santos, E.A. (2009): Numerical simulations of flows over a pair of cylinders at different arrangements using the immersed boundary method. *CMES: Computer Modeling in Engineering & Sciences*, vol. 50, no. 3, pp.285 – 303.

Dacles-Mariani, J.; Rogers, S.; Kwak, D.; Zilliac, G.G.; Chow, J.S. (1993): A computational study of wingtip vortex flowfield. *AIAA Paper 93-3010, Proc. 24th Fluid Dyn. Conf., Orlando, FL*.

Dacles-Mariani, J.; Zilliac, G.G.; Chow, J.S.; Bradshaw, P. (1995): A numerical/experimental study of a wingtip vortex in the near-field. *AIAA J.*, vol. 33, no. 9, pp.1561 – 1568.

Dacles-Mariani, J.; Kwak, D.; Zilliac, G. (1996): Accuracy assessment of a wingtip vortex flowfield in the near-field region. *AIAA Paper 96-0208, Proc. 34th AIAA Aerosp. Sci. Meet. & Exhib., Reno, NV*.

Gibson, M.M.; Launder, B.E. (1978): Ground effects on pressure fluctuations in the atmospheric boundary layer. *J. Fluid Mech.*, vol. 86, pp.491 – 511.

Jung, H.J.; Lee, J.H.; Rhee, S.H.; Song, M.; Hun, B.S. (2009): Unsteady flow around a two-dimensional section of a vertical axis turbine for tidal stream energy conversion. *Int. J. Naval Archi. & Ocean Eng.*, vol. 2, no. 2, pp.64 – 69.

Kim, S.-E.; Mathur, S.R.; Murthy, J.Y.; Choudhury, D. (1998): A Reynolds-averaged Navier-Stokes solver using unstructured mesh-based finite-volume scheme. *AIAA Paper 98-0231, Proc. 36th AIAA Aerosp. Sci. Meet. & Exhib., Reno, NV*.

Kim, S.-E. (2001): Unstructured mesh based Reynolds stress transport modeling of complex turbulent shear flows. *AIAA Paper 2001-0728, Proc. 39th AIAA Aerosp. Sci. Meet. & Exhib., Reno, NV*.

Kim, S.-E.; Rhee, S.H. (2002): Assessment of eight turbulence models for a three-dimensional boundary layer involving crossflow and streamwise vortices. *AIAA Paper 2002-0852, Proc. 40th AIAA Aerosp. Sci. Meet. & Exhib., Reno, NV*.

Kim, S.-E.; Rhee, S.H.; Cokljat, D. (2003): Application of modern turbulence models to vortical flow around a 6:1 prolate spheroid at incidence. *AIAA paper 2003-0429, Proc. 41st AIAA Aerosp. Sci. Meet. & Exhib., Reno, NV*.

Launder, B.E.; Shima, N. (1989): Second moment closure for the near-wall sub-layer: development and application. *AIAA J.*, vol. 27, no. 10, pp.1319 – 1325.

Lucas, P.; van Zuijlen, A.H.; Bijl, H. (2009): An automated approach for solution based mesh adaptation to enhance numerical accuracy for a given number of grid cells. *CMES: Computer Modeling in Engineering & Sciences*, vol. 41, no. 2, pp.147 – 175.

Mathur, S. R.; Murthy, J. Y. (1997): A pressure-based method for unstructured meshes. *Numer. Heat Transf. Part B. Fundam.*, vol. 31, no.2, pp.195 – 215.

Menter, F.R. (1994): Two-equation eddy-viscosity turbulence models for engineering applications. *AIAA J.*, vol.32, no.8, pp.1598 – 1605.

Naj, H.; Mompean, G. (2009): Computation of the turbulent flow in a square duct using a cubic low-Reynolds stress model. *CMES: Computer Modeling in Engineering & Sciences*, vol. 53, no. 2, pp.181 – 206.

Spalart, P.R.; Allmaras, S.R. (1992): A one-equation turbulence model for aerodynamic flows. *AIAA Paper 92-439, Proc. 30th AIAA Aerosp. Sci. Meet. & Exhib., Reno, NV.*

Shih, T.-H.; Liou, W.W.; Shabbir, A.; Zhu, J. (1995): A new k- ϵ eddy-viscosity model for high Reynolds number turbulent flows – model development and validation. *Comput. Fluids*, vol. 24, no. 3, pp.227 – 238.

